Environmental Science Nano

Effects of Nanoconfinement and Surface Charge on Iron Adsorption on Mesoporous Silica

Journal:	*Environmental Science: Nano*
Manuscript ID	EN-ART-01-2021-000066.R1
Article Type:	Paper

Nanopores are prevalent in nature, but their role in controlling the adsorption and transport of aqueous species has not been well explored. The effect of nanopores on aqueous chemistry is difficult to incorporate into geochemical models of solute adsorption and transport due to the variability of pore sizes in natural samples. Here we combine molecular simulation with X-ray adsorption spectroscopy to investigate pore size effects and nanoconfinement on the adsorption and surface complexes of an environmentally relevant metal cation (iron). We use synthetic silica materials and corresponding molecular models so that pore size can be carefully determined. The results demonstrate that iron adsorption is greatly enhanced on negatively charged surfaces. Adsorption also increases as pore size decreases, and in the presence of hydroxide anions which promote ion pairing and iron dimer formation. This work provides molecular-level explanations for the effects of aqueous chemistry, pore size, and nanoconfinement on iron adsorption.

Effects of Nanoconfinement and Surface Charge on Iron Adsorption on Mesoporous Silica

Jeffery A. Greathouse[1], Tyler J. Duncan[1], Anastasia G. Ilgen[1], Jacob A. Harvey[1], Louise J. Criscenti[1], and Andrew W. Knight[2]

[1]Geochemistry Department, Sandia National Laboratories, Albuquerque, NM 87185-0754, United States

[2]Storage and Transport Technologies Department, Sandia National Laboratories, Albuquerque, NM 87185-0754, United States

*Corresponding author. E-mail jagreat@sandia.gov

ABSTRACT

We present a combined molecular dynamics (MD) simulation and X-ray absorption fine structure (XAFS) spectroscopic investigation of aqueous iron adsorption on nanoconfined amorphous silica surfaces. The simulation models examine the effects of pore size, pH (surface charge), iron valency, and counter-ion (chloride or hydroxide). The simulation methods were validated by comparing the coordination environment of adsorbed iron with coordination numbers and bond lengths derived from XAFS. In the MD models, nanoconfinement effects on local iron coordination were investigated by comparing results for unconfined silica surfaces and in confined domains within 2 nm, 4 nm, and 8 nm pores. Experimentally, coordination environments of iron adsorbed onto mesoporous silica with 4 nm and 8 nm pores at pH 7.5 were investigated. The effect of pH in the MD models was included by simulating Fe(II) adsorption onto negatively charged SiO_2 surfaces and Fe(III) adsorption on neutral surfaces. The simulation results show that iron adsorption depends significantly on silica surface charge, as expected based on electrostatic interactions. Adsorption on a negatively charged surface is an order of magnitude greater than on the neutral surface, and simulated surface coverages are consistent with experimental results. Pore size effects from the MD simulations were most notable in the adsorption of Fe(II) at deprotonated surface sites (SiO^-), but adsorption trends varied with concentration and aqueous Fe speciation. The coordination environment of adsorbed iron varied significantly with the type of anion. Considerable ion pairing with hydroxide anions led to the formation of oligomeric surface complexes and aqueous species, resulting in larger iron hydroxide clusters at higher surface loadings.

Keywords: nanoconfinement, iron, amorphous silica, XAFS, molecular dynamics simulations

ENVIRONMENTAL SIGNIFICANCE

Nanopores are prevalent in nature, but their role in controlling the adsorption and transport of aqueous species has not been well explored. The effect of nanopores on aqueous chemistry is difficult to incorporate into geochemical models of solute adsorption and transport due to the variability of pore sizes in natural samples. Here we combine molecular simulation with X-ray absorption spectroscopy to investigate pore size effects and nanoconfinement on the adsorption and surface complexes of an environmentally relevant metal cation (iron). We use synthetic silica materials and corresponding molecular models so that pore size can be carefully controlled. The results demonstrate that iron adsorption is greatly enhanced on negatively charged silica surfaces. Adsorption also increases as pore size decreases, and in the presence of hydroxide anions which promote ion pairing and iron dimer formation. This work provides molecular-level explanations for the effects of aqueous chemistry, pore size, and nanoconfinement on iron adsorption.

INTRODUCTION

Nanoconfinement plays an important role in interfacial structure and reactivity of solid-water interfaces.[1-11] For aqueous systems, nanoconfinement affects the structural and transport properties of water, including density,[12] hydrogen bonding networks as evidenced by changes in vibrational properties,[13-15] and dynamic properties.[16-18] These deviations in water properties, induced by nanoconfinement, likely play a significant role in the abnormal behavior of solute species observed in nanoconfinement,[3] which could impact the fate and transport of environmentally relevant nutrients and contaminants.

Nanopores are ubiquitous in the environment, yet most geochemical models of solute adsorption and transport only consider the solid-fluid interface without including pore size (nanoconfinement) effects. This is because the pore size distribution of sedimentary rocks and soils can only be determined from laboratory measurements of field samples, and due to the wide range of pore-size distributions, the exact contribution on interfacial processes from nanopores is difficult to quantify.[19,20] Also, batch adsorption experiments are typically performed at higher water/sediment ratios than in natural rocks.[5] Alternatively, molecular simulation is well suited to improve our conceptual understanding of geochemical interfaces at the atomic, nano-, and meso-scales, thus providing a link between laboratory-scale and field-scale experiments and modeling. When benchmarked by molecular-scale spectroscopic observations, these simulations provide the necessary mechanistic insight. For example, previous studies of water H-bond dynamics in nanoporous silica indicate that water vibrational properties depend on distance from the surface rather than pore size.[21,22]

Here we use molecular dynamics (MD) simulations to systematically evaluate nanoconfinement effects on aqueous iron adsorption in amorphous silica nanopores due to changes in pH (surface charge), iron valency, solution composition (iron concentration, type of anion), and pore size (2 – 8 nm). Nanoconfinement introduces the effects of overlapping electric double layers that are important in coagulation and flocculation. In addition, nanoconfinement in tight rocks like shales may influence the formation of Fe-oxide coatings on quartz and silica surfaces.[23,24]

In our study, MD results are validated with batch adsorption experiments and X-ray absorption fine structure spectroscopy (XAFS). Because pore size is difficult to control in natural mineral samples, experiments were performed using the Santa Barbara Amorphous (SBA-15) class of mesoporous silicas with well-controlled pore diameters.[25,26] The pore walls of these materials are composed of amorphous silica with a surface hydroxyl coverage of approximately 2 $OH \cdot nm^{-2}$,[15] which is significantly less than the theoretical maximum for nonporous silicas[27] or quartz.[28] The pore size of these materials can be controlled during synthesis, resulting in materials with a narrow distribution of pore sizes as low as 2 nm.[29] For neutral pH conditions, in which the silica surface should be negatively charged,[30,31] we simulate the adsorption of Fe(II) at deprotonated SiO^- sites. We also model the adsorption of Fe(III) on neutral surfaces, corresponding to acidic conditions.

The present work builds on our previous MD simulation and experimental investigation of aqueous Cu(II) coordination and lanthanide Ln(III) adsorption in SBA-15 materials.[32,33] In that work, we developed SBA-15-like surface models of amorphous silica that are compatible with the ClayFF parameter set for simulating mineral-fluid interfaces.[34] These nonplanar surfaces contain a variety of bridging (siloxane) oxygen and surface hydroxyl (silanol) sites resulting

from the uneven nature of the surface. Additionally, the hydroxyl surface density closely matches the measured surface properties of SBA-15 materials. Although other amorphous silica surface models have been developed for MD simulation studies,[35-47] no other model has been specifically developed to represent SBA-15 materials.

METHODS

Computational Methods

All simulations were performed with the LAMMPS code.[48] Timesteps of 0.5 fs for short-range interactions (10.0 Å cutoff radius) and 1.0 fs for long-range electrostatic interactions were evaluated with a particle-particle particle-mesh algorithm.[49] Temperature was controlled using a Nose-Hoover thermostat with a relaxation time of 100 fs. The ClayFF parameter set[34] was used to model the fully flexible silica slabs. ClayFF is a nonbonded force field (FF) based on interatomic van der Waals and electrostatic interactions that has been used to simulate silicate phases including silica[35,42,50-54] and quartz.[55-61] The only bonded energy terms used for the silica model include a harmonic O-H bond stretch term included in ClayFF for layer hydroxyl groups, and a newly developed and experimentally validated Si-O-H angle bending term.[62,63] It is important to note that the nonbonded Si-O interaction is still included in the energy calculation involving Si-O-H groups. Importantly, both neutral and negatively charged models are stable during simulation under dry or wet conditions with full flexibility maintained. The flexible simple point charge (SPC) model[64] was used for water, and ion-water potentials for Fe(II), OH^-, and Cl^- were taken from the literature.[65-67] Since our focus is on determining the effects of

electrostatics on cation adsorption, FF parameters for the Fe(III) cation were the same as Fe(II) except that the charge was increased to +3 *e* (elementary charge). This approximation is justified based on nearly identical van der Waals energy profiles for Fe(II)-water and Fe(III)-water interactions.[68] Lennard-Jones parameters for unlike atom pairs were generated using arithmetic mixing rules. Representative input files with all interaction parameters are included in the Electronic Supplementary Information (ESI).

The amorphous silica slab was created by annealing a bulk β-cristobalite model as described in detail in our previous paper.[32] Briefly, the bulk sample was heated to 4000 K to produce a melted silica slab. After cooling the two-dimensional slab to 300 K, the rough surfaces were hydroxylated by satisfying undercoordinated silicon and oxygen sites with hydroxyl groups and hydrogen atoms, respectively. The surface hydroxyl density was then adjusted to 1.95 $OH \cdot nm^{-2}$ to match the experimental SBA-15 samples. This was accomplished by breaking additional Si-O bonds and water added across the bond to produce two new surface hydroxyl groups. The neutral model contains 2658 slab silicon atoms, 5625 slab oxygen atoms, and 222 silanol groups, with dimensions 65.7 × 65.8 × 38.2 $Å^3$ and a total surface area (both sides) of 138 $m^2 \cdot g^{-1}$. Negatively charged surfaces were created by removing 17 randomly chosen hydrogen atoms on each surface (−0.25 $C \cdot m^{-2}$), corresponding to experimental conditions (pH 7.5). The resulting −1.0 *e* charge at each site was distributed over the remaining silicon and oxygen atoms, creating a siloxide site. Simulation studies on similar surfaces have confined the negative charge exclusively to the siloxide oxygen site,[52] but to our knowledge a detailed comparison of charge delocalization schemes based on ClayFF silica models has not been performed.

A series of nanopore models were created and filled with Fe(II) or Fe(III) cations, chloride or hydroxide anions, and water. Fe(II) cations were simulated in the negatively charged pores

corresponding to higher pH (corresponding to the experimental measurements), while Fe(III) cations were simulated in the neutral pores corresponding to lower pH. For reference, the point of zero charge (PZC) for SBA-15 has been estimated to be 4.2.[69] Water molecules were first inserted into the pore in a grid pattern. Specific amounts of water corresponding to pore diameters of 2 nm, 4 nm, and 8 nm were determined from preliminary simulations with water-filled pores. Due to the roughness of the silica surfaces, average pore diameters were calculated by mapping the pore diameter along linear trajectories through the pore using the HOLE code.[70] Next, ions were randomly inserted into the pore, and any overlapping water molecules were removed (approximately 0.05 – 0.85 waters/ion). The number of cations was varied to achieve concentrations of approximately 0.05 M, 0.1 M, and 0.5 M. Even the lowest of these cation concentrations is much greater than that used in the experiments (1 mM), but as shown below the simulated and experimental surface loadings are similar, and the aqueous concentrations after adsorption are much lower than the bulk concentrations. For the negatively charged pore, an additional 17 Fe(II) cations were inserted to balance the surface charge. The number of anions (Cl^- or OH^-) was varied to maintain charge balance in the entire simulation cell. For the nonporous systems, the same number of water molecules for the 8-nm pores was used. Half of the water molecules and ions were inserted near each surface, and a Lennard-Jones wall located approximately 5 Å beyond the fluid layer kept the fluid species confined to the interfacial region. Special two-dimensional slab boundary conditions were used for the nonporous systems (kspace_modify slab command in LAMMPS) which removes dipole inter-slab interactions.[71] Exact composition of each model system is given in the ESI (Table S1), and representative snapshots of nanopore and nonporous models are shown in Figure 1.

Following an initial energy minimization to relax high energy intermolecular interactions due to close contacts, the pore fluid was equilibrated during a series of 200-ps *NVT* simulations as follows: 1) water molecules only at 500 K; 2) all fluid species with temperature ramp 500 K – 1000 K; 3) all fluid species at 1000 K; 4) all fluid species with a temperature ramp 1000 K – 300 K; 5) all fluid species at 300 K. The pore size was then equilibrated during a 1-ns *NPT* simulation at 300 K and 1 atm in which only the *z*-dimension of the simulation cell was allowed to vary. Finally, a 10-ns production *NVT* stage at 300 K was used for analysis. No *NPT* stage was run for the nonporous systems due to the 2D periodicity. Instead, an additional 1-ns *NVT* stage was run before the 10-ns production stage.

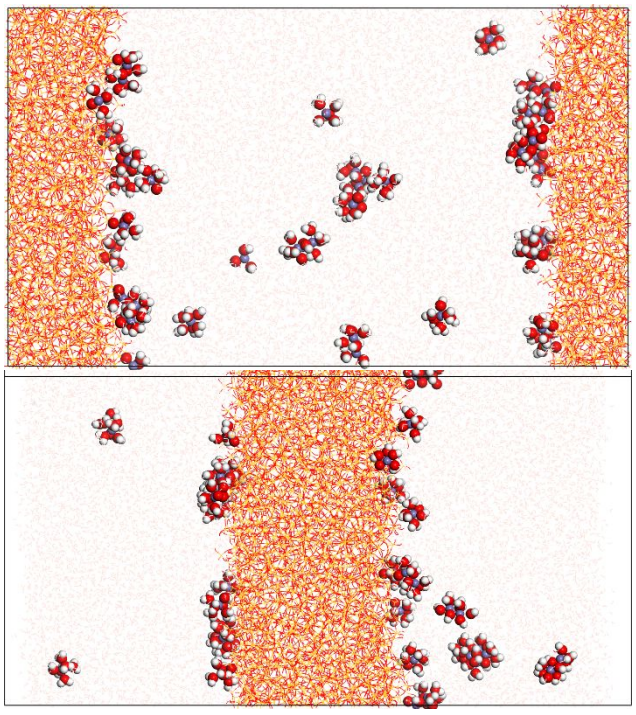

Figure 1. Snapshots showing simulation cells for 8 nm porous (top) and nonporous (bottom) models. Simulation cell boundaries are shown as black lines. Atoms are colored Fe (blue), O (red), H (white), Si (yellow). Fe coordination shells are shown as large spheres. Water molecules are lightly shaded for clarity.

Additional simulations were performed on charge-neutral bulk fluids (cubic boxes) of either Fe(II) or Fe(III) cations with hydroxide anions corresponding to the 8 nm pore volume. The number of water molecules were approximately the same as that of the 8 nm pore fluids (11,749 – 11,967 waters), with cation concentrations corresponding to 0.05 M, 0.1 M, and 0.5 M. After *NPT* equilibration, the actual concentrations were slightly higher (0.06 M, 0.11 M, 0.58 M), but for clarity pore fluids will be discussed in terms of their target concentrations.

Experimental Methods

All reagents used were ACS reagent grade or higher, including ferrous sulphate ($FeSO_4$), nitric acid (HNO_3), and HEPES buffer ($C_8H_{18}N_2O_4S$). Ultrapure HNO_3 was used for aqueous sample preservation and sample dilution prior to aqueous analysis (2 v/v %). Milli-Q H_2O (Barnstead NANOpure Diamond) with a resistivity of 18.2 MΩ*cm, 0.2 μm filtered and UV irradiated was used in the preparation of all solutions and suspensions.

Mesoporous SBA-15 silicas with reported pore diameters of 8-nm and 4-nm were purchased from Sigma Aldrich. We refer to these materials as SBA-15-8 and SBA-15-4 throughout the manuscript, corresponding to the approximate pore diameter of the material. These mesoporous silicas are amorphous and have hexagonally ordered cylindrical pores with measured diameters of 4.4 ± 0.3 and 7.0 ± 0.1 nm.[2] Purchased silica materials were washed in Milli-Q H_2O and dried in the oven at 45 °C for 48 hours or longer, as described previously.[2] As we reported earlier, the hydroxyl (-OH) site densities on the surfaces of mesoporous silicas were 1.8 ± 0.2 OH/nm^2 and 2.3 ± 0.2 OH/nm^2 for the SBA-15-8 and SBA-15-4, respectively. The BET surface areas were 580 m^2/g for SBA-15-4 and 661 m^2/g for SBA-15-8.[2]

Adsorption experiments were performed in batch reactors. Prior to adsorption, 200 ± 5 mg of dried silica material was equilibrated with 50 mL of Milli-Q H_2O for 24 hours. Then the background electrolyte and stock solutions were added. For adsorption samples, 10 mM HEPES buffer background electrolyte and $FeSO_4$ stock solution were used, and the starting aqueous concentration of Fe was 1.0 mM. The pH was not adjusted and was buffered by the HEPES solution at 7.5 ± 0.1. Then samples were placed on a mixing table or end-over-end rotator and reacted overnight. After reaction, samples were centrifuged at 3000 rpm for 10 minutes, and solid and liquid phases were separated. The supernatant was filtered using a syringe filter with 0.2-micron nylon membrane and acidified with ultrapure HNO_3. Aqueous concentrations of Fe after the adsorption experiments were quantified using inductively coupled plasma mass spectrometry (ICP-MS: NexION 350D). Analyses were run in collision mode, with helium gas flow set at 4-5 mL min^{-1}.

To preserve Fe(II) in adsorption samples they were mounted inside an anoxic glovebox (96% N_2 and 4% H_2 mixture) equipped with a palladium oxygen-scrubbing catalyst and oxygen O_2(g) sensor with the detection limit of 1 ppm. As we discuss below, the adsorption samples contain a mixture of Fe(II) and Fe(III) and the ratio of iron species is quantified using XAFS.

XAFS data were collected at the undulator beamline sector 20-ID (XOR) at the Advanced Photon Source (APS) at Argonne National Laboratory. An uncollimated beam was used with a Si(111) monochromator detuned by 30% for harmonic rejection. The monochromator was calibrated at the Fe K-edge at 7110 eV using an Fe metal foil. The monochromator step size was 10 eV in the pre-edge, with a counting time of 0.5 seconds per point, 0.3 eV step size in the near edge region with 0.5 second counting time, and 0.05 eV in the XAFS region with a counting time of 0.5 seconds per point. The fluorescence points for samples

were collected on a Vortex Si Drift solid state 4 element detector. For analyzing standards, we collected transmission spectra using an ionization chamber filled with helium. During the analysis, the sample chamber was kept at 22 K using a Displex liquid helium cryostat to avoid beam damage and the oxidation of Fe(II) to Fe(III). For each sample, between three and fifteen XAFS scans were collected to achieve an optimal signal to noise ratio. The Fe standards used to determine the oxidation state of Fe were iron (II) chloride ($FeCl_2$), iron (II) sulfate ($FeSO_4$), and iron (III) oxide (Fe_2O_3, amorphous), all purchased from Sigma Aldrich. The amplitude reduction factor (S_0) was determined to be 0.99 by fitting the Fe XAFS spectrum for the Fe_2O_3 standard. This S_0 value was used for fitting all Fe XAFS data collected during this analytical run.

The Fe K-edge XAFS data was processed and analyzed using Athena and Artemis [72] interface to the IFEFFIT software package.[73] The background subtraction, normalization, and conversion into k-space using Athena are described in detail elsewhere.[73,74] A Fourier transform (Hanning Window, dk = 2) was applied to the Fe K-edge XAFS data over the k-range from approximately 3 – 11. The Fourier transformed data was imported to Artemis to be analyzed by IFEFFIT[72] with a shell-by-shell fitting of theoretical single scattering (SS) paths approach.[75] The theoretical phase and amplitude functions for Fe-O, Fe-Fe, and Fe-Si single scattering paths were generated using the FEFF6 code[75] from the crystal structure of nontronite, $Na_{0.5}Fe_2(Si_{3.464}Al_{0.536})O_{12}H_2$, reported by Manceau et al.[76]

RESULTS

Iron adsorption from MD simulations

One of the many complexities in comparing experimental adsorption data to MD simulations is that due to computational limitations, simulations are inevitably performed using a higher concentration of solute than used in the experiments. In our simulations, the higher concentrations resulted in the formation of iron hydroxide oligomers, which is consistent with Fe(III) speciation in natural waters at higher pH[77] and the precipitation of Fe(II) hydroxide at pH 7.8.[78]

We first examine pore size and anion effects on iron adsorption. Figure 2 shows adsorption isotherms for Fe(II) and Fe(III) on the charged and neutral silica surfaces, respectively. Surface coverages were calculated from nearest neighbor Fe-O_{pore} atomic density profiles, considering all iron atoms within 5.0 Å of a surface oxygen atom (O_{pore}) as "adsorbed". Note that O_{pore} can be a siloxide oxygen, siloxane oxygen, or silanol oxygen atom. These density profiles are discussed in more detail below, but we note that the 5.0 Å value for adsorption includes both inner-sphere (IS) and outer-sphere (OS) complexes as well as iron oligomers in the interfacial region. Uncertainties in adsorbed amounts cannot be determined from single MD trajectories, but a similar study using ten replicate trajectories showed uncertainties in adsorption to be approximately 10 %.[79]

Based on the slope of the adsorption isotherms, iron adsorption has not reached maximum loading at the highest concentration (0.5 M), indicating that not all available silica adsorption sites are occupied by iron. Most noticeable in the adsorption trends is the drastically lower Fe(III) adsorption (Figures 2C and 2D) compared to Fe(II) adsorption (Figures 2A and 2B), which is primarily due to surface charge effects. Only the Fe(II) systems included a negatively charged surface, while the neutral surface used in the Fe(III) systems contained no deprotonated SiO^- sites. Separate simulations with a 0.1 M $Fe(OH)_2$ solution near a neutral

surface (4-nm pore) and a 0.1 M $Fe(OH)_3$ solution near a charged surface confirmed the role of surface charge in cation-surface interactions. Adsorption at the neutral surface was reduced by an order of magnitude compared to the negatively charged surface for both Fe(II) and Fe(III). We know from bulk adsorption experiments[80] that Fe(III) adsorption on silica occurs at low pH, perhaps even below the point of zero charge (PZC), which is 4.2 for SBA-15.[69]

The Fe(II) concentrations shown in Figure 2 correspond to the initial concentration of the pore fluid and were not corrected for the amount adsorbed. However, we provide a detailed accounting of Fe(II) cations (adsorbed and aqueous) in Table S2. The adsorption of Fe(II) cations resulted in a significant decrease in free (aqueous) cations, particularly for the 0.05 M and 0.1 M fluids. Figure 2 and Table S2 also highlight the effect of anions on adsorption.

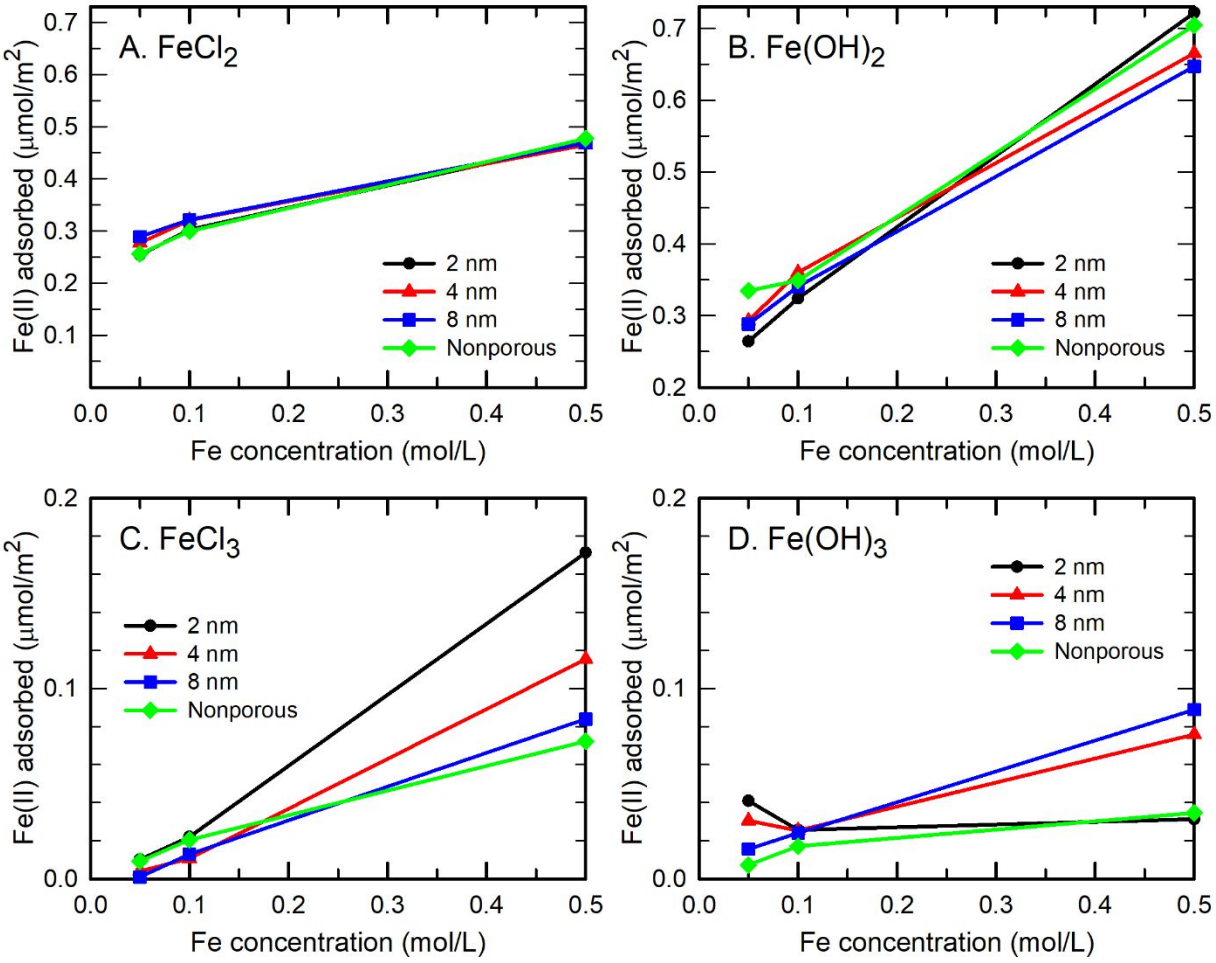

Figure 2. Fe(II) and Fe(III) adsorption isotherms from MD simulations in silica nanopores as a function of pore size and iron concentration. A) $FeCl_2$ and B) $Fe(OH)_2$ at the charged surface, C) $FeCl_3$ and B) $Fe(OH)_3$ at the neutral surface (no siloxide sites). All iron cations within 5.0 Å of a surface oxygen atom were considered to be adsorbed.

Representative Fe(II) IS surface complexes are shown in Figure 3, in which Fe(II) cations are coordinated to deprotonated SiO^- sites (O_{dep}). The strong tendency for hydroxide-coordinated oligomer formation in the 0.5 M hydroxide systems results in increased adsorption compared to the chloride systems. As shown in a summary of Fe-O(H) and Fe-Cl coordination numbers (CNs) from radial distribution function (RDF) analysis (Tables S3 – S6), Fe-hydroxide ion pairs are more likely to form than Fe-chloride ion pairs. One or more Fe(II) cations in hydroxide-

coordinated oligomers can bind to surface siloxide sites (Figures 3B and 3C), resulting in significantly increased adsorption compared to the chloride systems.

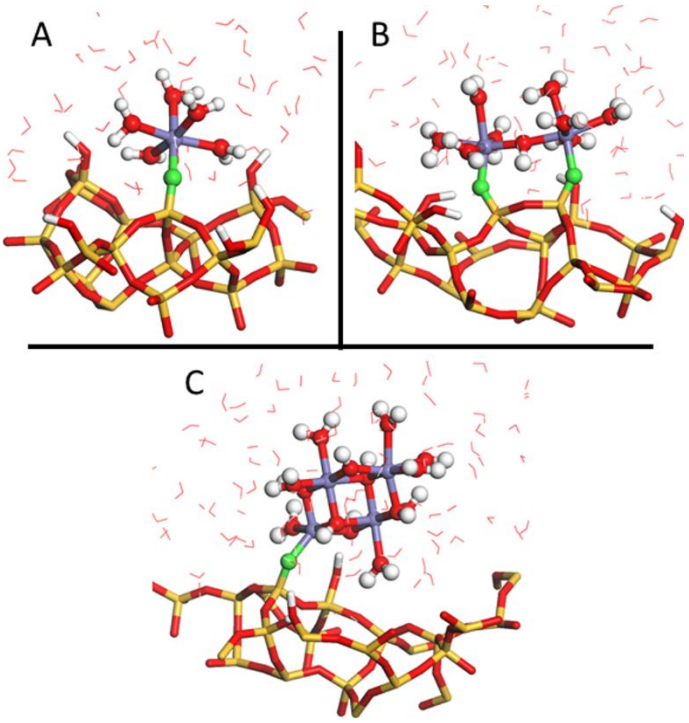

Figure 3. Snapshots showing A) monomer, B) dimer, and C) tetramer Fe(II) complexes adsorbed on the negatively charged silica surface. A) $Fe(O_{dep})(OH_2)_5$, B) $Fe_2(O_{dep})_2(OH)(OH_2)_8$, C) $Fe_4(O_{dep})(OH)_4(OH_2)_8$. Atom colors are the same as Figure 1 except that O_{dep} atoms are green.

The surface concentrations in Figure 2 include IS adsorption at specific surface sites (*e.g.*, O_{dep}) but also other iron cations within 5 Å of the surface from OS surface complexes or from adsorbed Fe oligomers. An alternate method of examining trends in Fe(II) adsorption is by comparing the fraction of occupied adsorption sites. For the negatively charged surface, fractions of SiO^- sites occupied by Fe(II) at a Fe-O distance of approximately 2.0 Å (IS complexes) were obtained from CNs from RDF plots (Tables S3 – S6). These fractions are plotted for all Fe(II) systems in Figure 4. The fraction of SiO^-sites occupied by Fe(II) increases with concentration, as

expected when considering the effect of solute concentration on adsorption at specific sites. For reference, the Fe(II)/O_{dep} ratios for each system are shown in Table 1. It is of interest to note that when the SiO^- site occupancy surpasses 0.5—as is the case for all results in Figure 4—the net charge due to adsorbed Fe(II) is greater than the surface charge. However, the presence of anions coordinated to these cations (Tables S3 and S5) likely results in a neutral or negative net surface charge. Trends in SiO^- site occupancy with pore size are consistent with adsorption results (Figure 2) for chloride anions but not for hydroxide anions. These differences are likely due to adsorbed iron oligomers in the hydroxide systems, as discussed in more detail below.

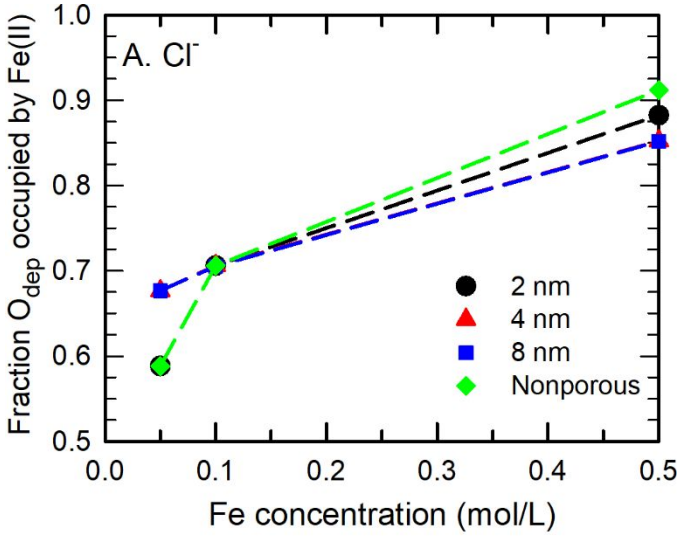

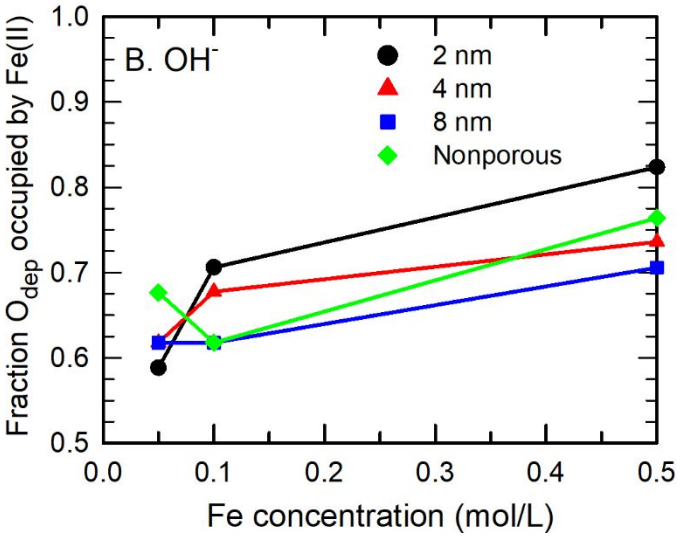

Figure 4. Fraction of siloxide sites occupied by Fe(II) cations from MD simulations in negatively charged silica nanopores as a function of pore size and iron concentration. Results are shown for A) chloride and B) hydroxide anions. Any siloxide O atom within 2.2 Å of an Fe^{2+} ion was considered occupied.

Table 1. Fe(II)/O_{dep} Ratios in the MD Models

pore size	0.05 M	0.1 M	0.5 M
2 nm	0.65	0.79	1.97
4 nm	0.74	0.94	2.71
8 nm	0.88	1.24	4.18
nonporous	0.88	1.24	4.18

We use atomic density profiles and iron speciation analysis to examine the effect of hydroxide-coordinated iron complexes on adsorption. Figure 5 shows specific contributions of iron monomers and oligomers to iron-surface atomic density profiles for 0.1 M iron solutions. Profiles for 0.05 M and 0.5 M solutions are shown in Figures S1 and S2. For planar interfaces, such profiles are typically plotted as a function of distance to the surface. For the nonplanar interfaces in our amorphous silica model, densities are instead plotted as a function of distance between iron cations and the nearest oxygen atoms along the pore wall (O_{pore}). Only monomer profiles are shown for the chloride systems since no Fe-Fe complexation was seen (Tables S3 and S5). Monomer profiles in Figure 5 reveal a consistent adsorption environment regardless of anion, but significant differences are seen depending on surface charge. Adsorption of Fe(II) monomers and oligomers occurs *via* IS surface complexation at an Fe-O_{dep} distance of approximately 2 Å, while Fe(III) monomers and oligomers generally adsorb on the neutral surface as OS surface complexes at Fe-O distances between 3.5 Å – 4.5 Å. Density peaks due to IS adsorption of Fe(II) on the negatively-charged surface shows a pore size dependence (2 nm > 4 nm > 8 nm), which is consistent with the trend of SiO^- site occupancy (Figure 4B).

Some IS Fe(III) adsorption at Si-OH or Si-O-Si oxygen sites is seen for the nonporous system with hydroxide anion at all concentrations (Figures 5, S2, and S3), and also in some porous systems with chloride anion (Figures S1 and S2). However, the lack of consistency and very low Fe-O CNs (Tables S5 and S6) suggests that these are rare occurrences and not indicative of a dominant adsorption mechanism. In fact, Fe(III) is nearly excluded from the neutral surface, implying that the Fe(III) concentration in the adsorbed layer is lower than that of the original aqueous solution. Since Fe(III) is observed to adsorb readily to silica around the PZC,[80] further investigation is required to understand our results. For example, IS adsorption of Fe(III) at silanol sites can result in deprotonation (release of H^+), but this process cannot be modeled in our force field approach

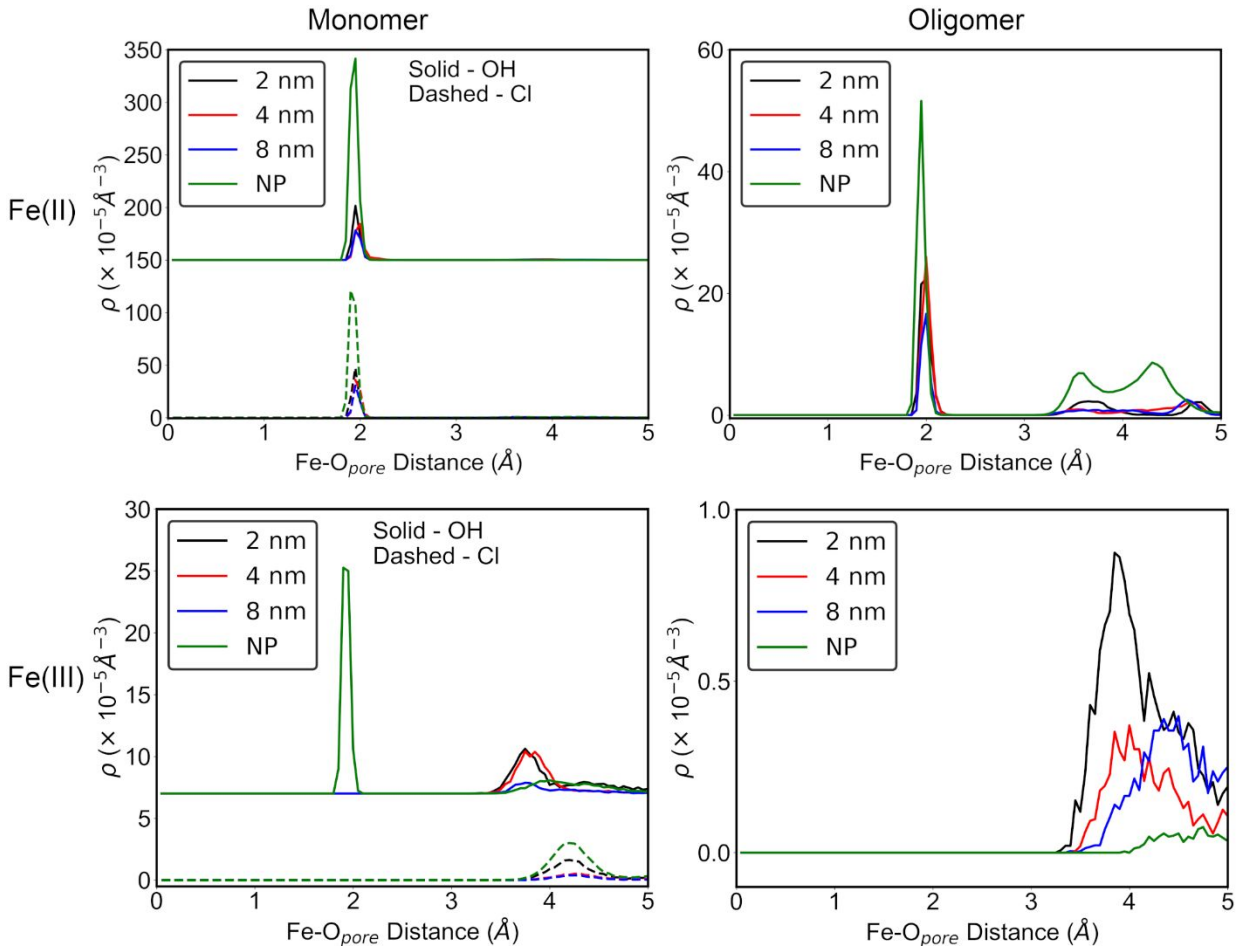

Figure 5. Atomic density profiles of the shortest distance between an iron cation and a surface oxygen atom (O_{pore}) as a function of pore size and anion (NP refers to nonporous). Results are shown for 0.1 M Fe(II) at the charged surface (top) and Fe(III) at the neutral surface (bottom). Profiles for iron oligomer adsorption (right) are shown for OH^- only since no oligomers formed in the Cl– systems.

The effect of pore size on oligomer formation is shown in a histogram analysis of iron oligomers from simulations of 0.1 M Fe(II) with hydroxide anions in negatively charged porous and nonporous silica models, and bulk Fe(II) and Fe(III) solutions with hydroxide anions at all concentrations (Figure S3). As the pore size increases from 2 nm to 8 nm, the monomer frequency decreases (0.86 for 2 nm to 0.68 for 8 nm) while the dimer frequency increases (0.10 to 0.29). The frequency of monomers in the nonporous system and bulk solution are even lower (0.65 and 0.43, respectively), but instead of mainly dimer formation, trimers, tetramers, and

pentamers are also seen. The increasing tendency to form oligomers in the 8 nm and nonporous systems results in less direct binding of Fe(II) cations to surface SiO^- sites (Figure 4B, 0.1 M) but not overall adsorption (Figure 2A).

Histograms for the bulk Fe(II) and Fe(III) fluids also show an increasing tendency to form oligomers as Fe concentration increases. Results for the 0.1 M bulk fluid and the 8-nm (and nonporous) fluids are similar, with a slight increase in frequency of larger Fe clusters in the bulk fluid. We did not attempt to determine if oligomers first formed in solution before adsorption, or if they formed after single cations first adsorbed. This is beyond the scope of our current study but could be the focus of a broader study on cation adsorption and nucleation. However, aqueous Fe(III) dimers have been studied using XAFS.[81] and oligomerization is a first step in iron oxyhydroxide formation.[82]

Iron Coordination and Structure

We used XAFS to characterize the local coordination environment around iron species adsorbed onto mesoporous silica surfaces at pH 7.5, where the silica surface is negatively charged. The resulting fits are summarized in Table 2 and Figure 6. We note that the iron adsorption loadings in the experimental samples (approximately 0.3 μmol/m^2 for both pore sizes) closely match the 0.05 M MD results (Figure 2, 0.25 – 0.33 μmol/m^2). While we protected the Fe(II) samples from exposure to atmospheric oxygen, we still observed that the majority of iron in these samples was Fe(III), likely due to the initial stock solution containing a mixture of these species. To quantify the ratio of Fe(II)/Fe(III) in our samples, we used linear combination fitting in the Athena program.[72] Fitting using pure Fe(III) and Fe(II) standards indicates that the SBA-15-8-Fe(II) sample contained 23% Fe(II) and 77% Fe(III), and the SBA-15-4-Fe(II) sample

contained 16% Fe(II) and 84% Fe(III). However, since the MD results clearly demonstrate that iron adsorption on silica is dominated by surface charge rather than cation valency, a comparison of iron coordination shell distances between MD results for Fe(II) and XAFS results for mixed Fe(II)/Fe(III) solutions is justified.

Table 2. Summary of X-ray absorption spectroscopy (XAFS) shell-by-shell fitting results. Fitting was done in R-space; k-weights of 1, 2, and 3 were fitted simultaneously, the amplitude reduction factor S_0 was 0.99. Error at a 95 % confidence level is shown in parenthesis.

Sample	Surf. conc, µmol/m^2	[1] k-range	R-range (Å) (uncorr)	Shell	[2] CN	[3] R (Å)	[4] σ^2 (Å^2)	[5] ΔE_0 eV	[6] R-factor	[7] Red χ^2	[8] Ind. Pts.
SBA-15-8 (pH 7.5)	0.290	3.0-9.74	1.0-3.3	Fe-O	2.4(4)	1.84(2)	0.003(2)	-4.2	0.037	605	13.8
				Fe-O	3.2(6)	2.06(1)	0.004(2)				
				Fe-Si	2.8(8)	3.26(2)	0.002(3)				
				Fe-Fe	1.7(6)	3.23(2)	0.002(2)				
SBA-15-4 (pH 7.5)	0.310	3.0-9.74	1.0-3.4	Fe-O	2.3(3)	1.87(1)	0.003(2)	-4.9	0.028	227	14.1
				Fe-O	2.4(4)	2.07(1)	0.002(1)				
				Fe-Si	3.1(6)	3.20(2)	0.001(2)				
				Fe-Fe	2.2(4)	3.19(2)	0.001(2)				

[1] Usable k-range
[2] Coordination number
[3] Bond length
[4] Debye-Waller factors: mean-square amplitude reduction factor, including thermal and static disorder components
[5] Energy shift between the theoretical and measured spectrum
[6] R-factor (mean square misfit) $R_{factor} = \frac{\sum_i (data_i - fit_i)^2}{\sum_i data_i^2}$
[7] Reduced chi-square $\chi_v^2 = \frac{N_{idp}}{N_{pts}} \sum_i \left(\frac{data_i - fit_i}{\varepsilon_i} \right)^2 / (N_{idp} - N_{var})$
[8] Independent points (number of data points minus number of variable parameters) $N_{idp} = N_{pts} - N_{var}$

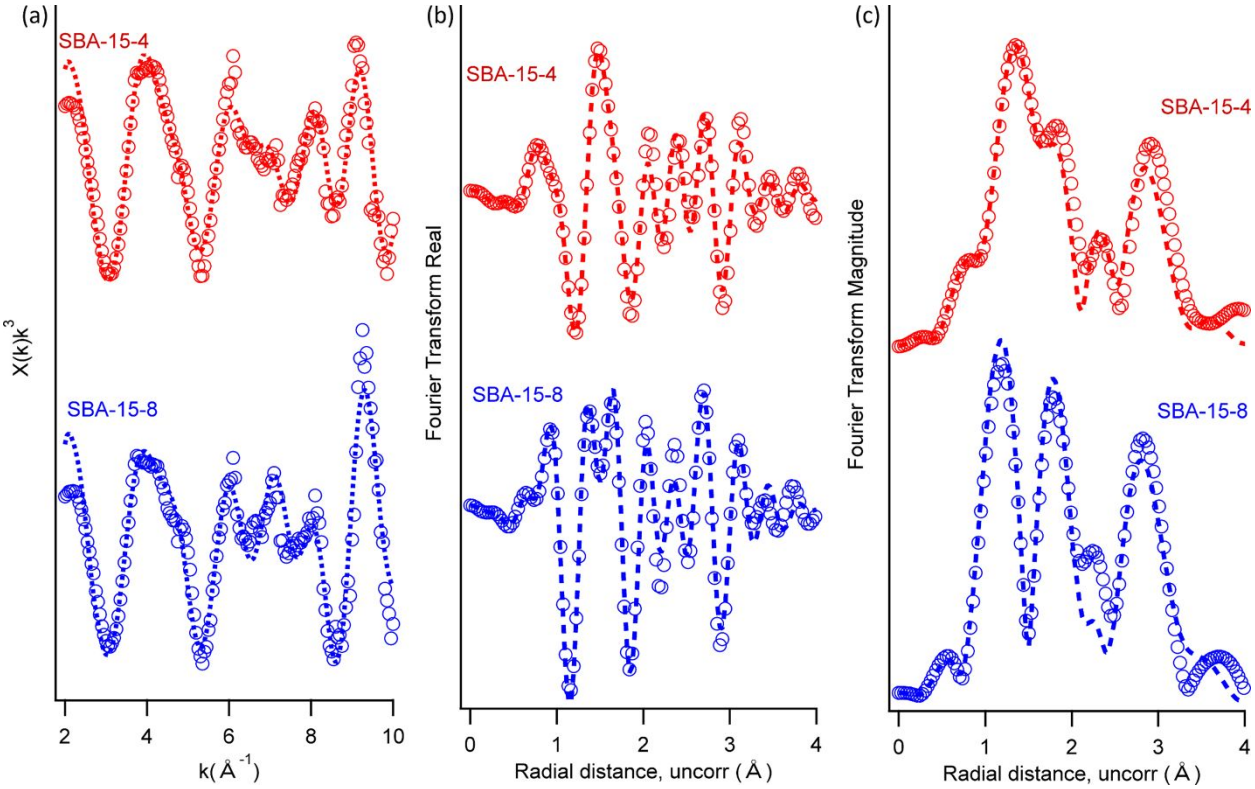

Figure 6. X-ray absorption fine structure spectroscopy (XAFS) data and shell-by-shell fitting results shown in k-space (a), magnitude of the Fourier transform (b), and the real part of Fourier transform (c). The symbols show the collected experimental data, and the lines are the corresponding fits.

We observed subtle differences in the local coordination environment as a function of pore size. Four shells were observed in the XAFS spectra. Two were fit with Fe-O backscattering paths, one with a Fe-Si path, and one with a Fe-Fe backscattering path, indicative of the presence of polynuclear iron species (or, potentially, the presence of a Fe(III) surface precipitate). The reason for the occasional mismatch between XAFS model and data, is that these iron adsorption samples are disordered, when compared to the crystalline compounds used in FEFF calculations of the theoretical backscattering paths used in the shell-by-shell fitting. Incomplete overlap between XAFS data and model have been seen in previous studies of adsorbed ions.[83,84] The Fe-Si distance of 3.20-3.26 Å is consistent with either a mono- or a bi-dentate surface complex. The Fe-Fe distance is consistent with an edge-sharing Fe(III) octahedron. For the 8-nm pores, the Fe-

O distances were 1.84 ± 0.04 Å and 2.06 ± 0.01 Å, while these same shells had slightly longer distances of 1.87 ± 0.01 and 2.07 ± 0.01 Å in 4-nm pores. The Fe-Si distances were slightly shorter for the 4-nm silica, compared to 8-nm (Table 2).

The Fe(II) and Fe(III) coordination environments from the MD simulations were obtained from analysis of averaged RDFs. MD results for 0.1 M Fe(II) with hydroxide anion are compared with XAFS in Table 3, although both Fe(II) and Fe(III) were present in the experimental samples. MD results for 0.05 M could have been used for the XAFS comparison, but the first shell distances and CNs are nearly identical at the two concentrations. All MD results for Fe(II) and Fe(III) are provided in Tables S3 – S6. Fe-O distances from MD are generally in agreement with XAFS, ranging from 1.85-1.97 Å for Fe-O(H) or Fe-O_{dep}, and 2.06 – 2.13 Å for Fe-O_w, where O(H) and O_w refer to hydroxide and water oxygens, respectively. The first shell iron CN in all MD systems (6) is similar to the 8 nm XAFS result (5.6), but the experimental CN is much lower (5.6) in the 4 nm pore. Previous XAFS studies of Fe(III) complexes in the presence of aqueous silica indicate that tetrahedrally coordinated Fe(III) can result when iron substitutes for silicon in the polymeric silica network.[85]

Table 3. Comparison of Fe First Shell Distances from MD[a] and XAFS.

surface charge ($C \cdot m^{-2}$)	Fe species (MD)	pore size (nm)	Shell[b]	MD		XAFS[c]	
				CN	R (Å)	CN	R (Å)
0	Fe(III)	8	Fe-O(H)	3.7	1.89		
			$Fe\text{-}O_w$	2.3	2.07		
			Fe-O	-	-		
			Fe-Fe	0.7	3.00		
			Fe-Si	-	-		
0	Fe(III)	4	Fe-O(H)	3.9	1.87		
			$Fe\text{-}O_w$	2.1	2.06		
			Fe-O	-	-		
			Fe-Fe	0.7	3.00		
			Fe-Si	-	-		
–0.25	Fe(II)	8	$Fe\text{-}O_{dep}$	0.5	1.97	2.4	1.84
			Fe-O(H)	1.8	1.97		
			$Fe\text{-}O_w$	3.6	2.13	3.2	2.06
			Fe-Fe	0.6	2.97	1.7	3.23
			Fe-Si	0.5	3.25	2.8	3.26
–0.25	Fe(II)	4	$Fe\text{-}O_{dep}$	0.7	1.97	2.3	1.87
			Fe-O(H)	1.5	1.97		
			$Fe\text{-}O_w$	3.7	2.13	2.4	2.07
			Fe-Fe	0.7	2.97	2.2	3.19
			Fe-Si	0.7	3.25	3.1	3.20

[a] MD results are shown for 0.1 M Fe(II) with hydroxide anions since the experimental systems did not contain chloride anions

[b] O_{dep} = deprotonated surface oxygen, O_w = water oxygen, O(H) = hydroxide oxygen

[c] XAFS samples were prepared at pH 7.5, which corresponds to a negatively charged surface

Plots of Fe-Fe RDFs from MD simulations aid in the interpretation of Fe-Fe CN values seen in Table 3. These are shown for 0.1 M Fe(II) and Fe(III) systems in Figure 7 (0.05 and 0.5 M are shown in Figure S4). The most common Fe-Fe distance from MD is approximately 3.0 Å, indicative of a dimeric complex with two bridging hydroxide ions (Figure 7A). This peak increases in intensity as pore size increases, indicating an increasing tendency for oligomer formation with more iron cations in the pore fluids. Other Fe-Fe distances are more prominent in the Fe(III) systems (Figure 7B), corresponding to Fe dimers bridged by three hydroxides (2.6 Å – 2.7 Å) or one hydroxide (3.6 Å – 3.7 Å). We note that the composition and first shell distances of these complexes are highly dependent on the iron FF parameters used, and these parameters were not adjusted to fit the XAFS distances.

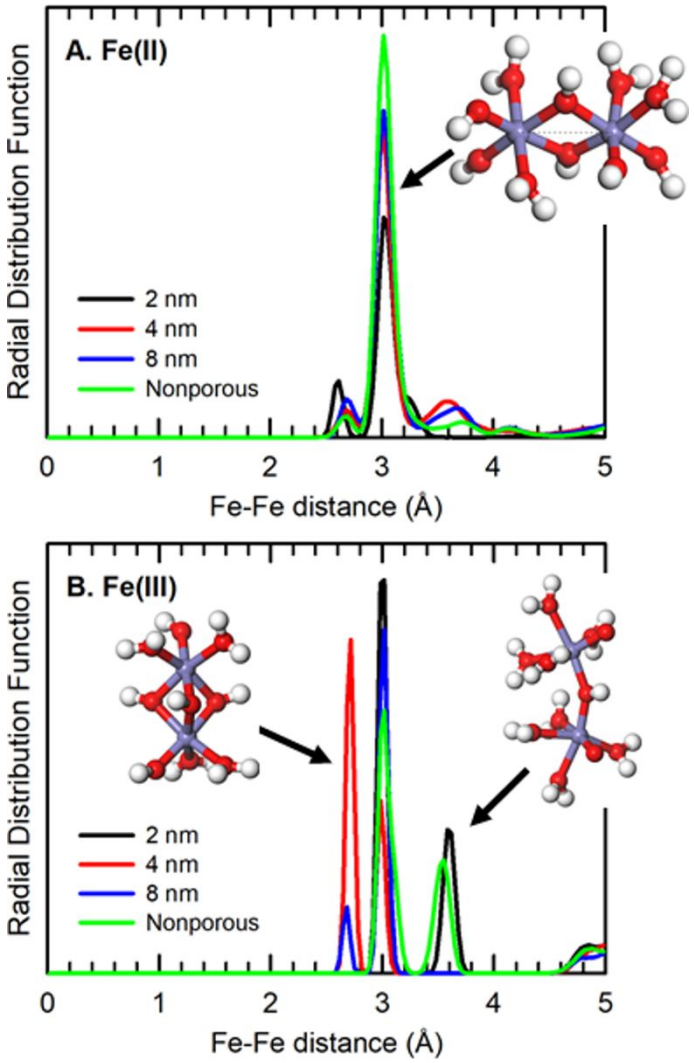

Figure 7. Illustration of Fe-Fe coordination from MD simulations of A) 0.1 M Fe(II) at a charged surface and B) 0.1 M Fe(III) at a neutral surface, both with hydroxide anion. Accompanying snapshots illustrate the indicated Fe-Fe distances.

No Fe-Fe complexes were seen in the chloride systems (Tables S3 and S5), but they were seen in the hydroxide systems at all pore sizes and iron concentrations (Tables S4 and S6), and in bulk hydroxide solutions (Figure S3). The XAFS data also indicated the presence of oligomeric species in both 4 nm and 8 nm pores. MD results for Fe(II) hydroxide near the charged surface indicate no consistent pore size dependence for Fe-Fe CNs, but they are more prevalent as concentration increases. Ranges of Fe-Fe CN values are 0.24 – 0.54 (0.05 M), 0.57 – 1.13 (0.1

M), and 2.35 – 3.31 (0.5 M). Note that a Fe-Fe CN greater than unity indicates the presence of oligomers, as illustrated in Figure 8. Additionally, the presence of even a single oligomer in the MD system can greatly alter the Fe-Fe CN. For example, the 2-nm pore at 0.1 M Fe(II) contains mostly monomers and dimers but also a single pentamer (Figure S3). Without these oligomers, the pore size trend in Fe-Fe CN would match the trend in monomer/dimer ratios. Although the Fe-O force field parameters used here were developed to model Fe(II) hydration, the formation of Fe(II) hydroxide clusters at higher concentrations suggests that these potentials could also be used to study mineral nucleation.[85,86]

We also note that the tendency to form Fe-Fe complexes also depends on surface charge. MD results for 0.1 M Fe(II) show that Fe-Fe coordination increases near the neutral surface (Table S4). With no ability to form IS surface complexes on the neutral surface, Fe-Fe CNs for 0.1 M Fe(II) in 4 nm pores increases from 0.69 (negatively charged surface) to 1.47 (neutral surface). The Fe(II)-hydroxide CN is also substantially larger at the neutral surface (3.12) compared to the charged surface (1.47). These comparisons suggest that surface charge likely influences the formation of surface precipitates.

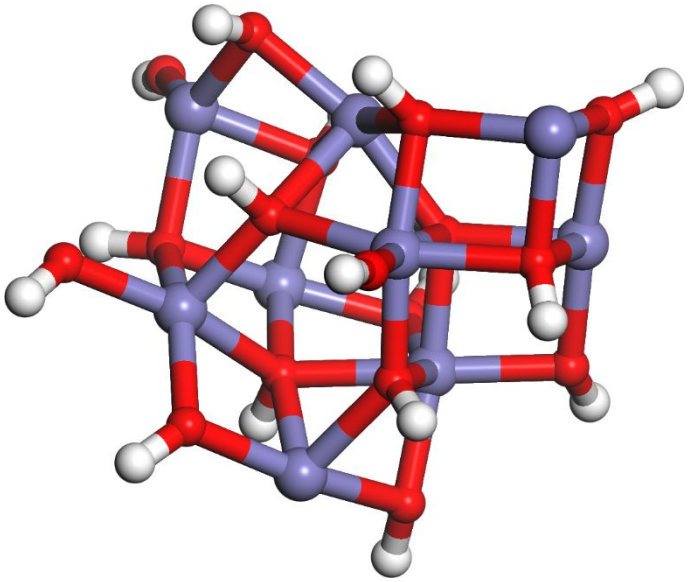

Figure 8. Snapshot from an MD simulation of 0.5 M Fe(II) with hydroxide anion, showing the onset of crystal nucleation. Coordinating water molecules have been removed for clarity.

DISCUSSION

Despite differences between the experimental and simulated systems, the amount of iron adsorbed on negatively charged surfaces is in close agreement, and the simulations reveal that this interaction is based largely on electrostatic interactions. This negative surface charge is likely to enhance the nanoconfinement effect due to surface-driven re-structuring of hydrogen bonding networks at the interface. While the correlation between surface charge and adsorption is expected, the link between nanoconfinement and surface charge effects requires detailed studies such as this to illustrate.

Our discussion of pore size effects on simulated Fe(II) adsorption will only focus on the lowest concentrations on the charged surface (0.05 M and 0.1 M in Figures 2A and 2B). While the iron concentration was much lower in the experiments (1.0 mM), both MD and experiment show iron surface concentrations of approximately 0.3 $\mu mol \cdot m^{-2}$. Regardless of anion in the MD

models, at the lower concentrations (0.05 M and 0.1 M) total Fe(II) surface concentration is reduced in the 2 nm pore compared to the larger pores (Figure 2). Nearly all cations in the (initially) 0.05 M and 0.1 M fluids are adsorbed in the 2 nm pore (Table S2), but the Fe(II) surface concentrations are less than for 0.5 M fluids or larger pores because there are fewer cations present in the 2-nm pores. When hydroxide ions are present, MD results show that Fe(II) surface concentrations are greater in the 4 nm pore than the 8 nm pore (Figure 2B and Table S1), which is due almost entirely to an increase in IS adsorption (Figure 4B). Importantly, both simulation and experiment demonstrate that iron adsorption increases slightly as the pore size decreases from 8 nm to 4 nm (Table 2).

Trends in SiO^- site occupation (Figure 4) facilitate a comparison of IS adsorption tendencies and serve to demonstrate the effect of increasing cation adsorption with decreasing pore size. The MD results also indicate that IS Fe(II) adsorption is significantly influenced by aqueous chemistry (type of anion). For all systems, the fraction of occupied SiO^- sites is lower—in most cases, significantly lower—than the Fe(II)/O_{dep} ratio (Table 1). Only for a few 0.05 M systems (2 nm and nonporous) is the fraction of occupied SiO^- sites similar to the Fe(II)/O_{dep} ratio, indicative of near total Fe(II) adsorption as IS surface complexes. The reduced Fe(II) surface concentrations in these systems is likely due to the fewer numbers of Fe(II) cations in the models. At higher Fe(II) concentrations of 0.1 M and 0.5 M, a reservoir of aqueous cations is available for adsorption, similar to batch experimental systems. We see from Figure 4B that IS adsorption in hydroxide solutions clearly shows a pore size dependence at these higher concentrations. This trend is in agreement with our previous study of Cu(II) adsorption on silica surfaces,[33] as well as our XAFS study of lanthanide adsorption in SBA-15 materials, in which nanoconfinement promotes inner-sphere adsorption.[33] There is little or no pore size effect for IS

adsorption in chloride solutions, which is likely due to the absence of Fe-Fe complexation (Tables S3 and S5). Overall, the MD results show that Fe(II) adsorption is influenced by both pore size and anions present in the solution.

The 8 nm MD models allow us to examine the effect of nanoconfinement on Fe(II) adsorption. The only difference in the porous 8 nm and nonporous models is the fluid boundary away from the silica surface, yet opposite adsorption trends are seen depending on the anion. For 0.05 M chloride solutions, Fe(II) surface concentration and IS adsorption is greater in the porous model, but for 0.05 M hydroxide solutions adsorption is greater in the nonporous model. The adsorption trends are the same as trends in Fe-O_{dep} CNs, but opposite of the trends in Fe-anion CNs (Tables S3 and S3). In other words, greater Fe-anion complexation results in more negative aqueous Fe(II) complexes, which are less likely to adsorb. Differences in Fe(II) speciation and adsorption between the porous and nonporous 8-nm systems could be due to the different fluid boundary (the nonporous model has a hydrophobic vacuum interface), small fluid thickness (4 nm on each side of the silica surface), or possibly a consequence of limited sampling data. Properties of the confined fluids should converge to those of the corresponding nonporous fluid as pore size increases. It is likely that larger pore sizes and thicker nonporous fluid layers would be required to see this convergence.

Additionally, no Fe-Fe complexes formed in the chloride systems, but they are seen in the hydroxide systems at all concentrations. Hydroxide-coordinated Fe(II) oligomers are strongly adsorbed via IS complexation with siloxide sites, resulting in a greater surface concentration of Fe(II) cations. This effect appears to enhance the adsorption of Fe(II) in the 8-nm nonporous hydroxide system compared to the porous counterpart. Combined with our previous studies of

ion adsorption on porous silica surfaces,[32,33] we see that nanoconfinement in the presence of charged surfaces changes the behavior of aqueous solute.

The XAFS results indicate that under nanoconfinement the hydration shell around adsorbed iron may become less tight, as indicated by slightly longer bond distances. Differences in composition and radii of the first coordination shells between XAFS and MD could be due to a number of factors, including differences in the fluids (concentration and composition), and surface adsorption geometries. Interestingly, CNs for the nonporous systems usually fall within the 4 nm and 8 nm values, even though the thickness of the aqueous region at each surface is closer to the 8 nm pore.

Differences in surface complex geometries could also account for differences in Fe-Si distances between MD and XAFS. Monodentate surface complexes seen in MD correspond to a Fe-Si distance of 3.25 Å, consistent with a slightly bent Si-O_{dep}-Fe angle as illustrated in Figure 3. A similar Fe-Si distance of approximately 3.20-3.26 Å is seen in XAFS. Adjacent charge sites were not included in the surface model, so there were no O_{dep} sites close enough to allow for bidentate $Fe(O_{dep})_2$ surface complexes.

CONCLUSIONS

We performed an extensive set of MD simulations of aqueous iron adsorption at amorphous silica interfaces, comparing the effects of iron valency, concentration, anion chemistry, and surface charge. In parallel, we used batch adsorption experiments and XAFS to examine local coordination environments as a function of pore size in SBA-15 mesoporous silica

with negative surface charge. The hydroxyl site density in the MD model closely matches that of the mesoporous silica materials used for XAFS analysis. The negatively-charged surface—corresponding to neutral pH conditions—contained deprotonated SiO^- sites, which resulted in significantly greater iron adsorption compared to the neutral surface (lower pH). Both XAFS and MD results indicate that iron adsorption at SiO^- sites occurs via IS surface complexes. The MD results further revealed that IS adsorption increases with decreasing pore size when hydroxide ions are present. As hydroxide concentration increases, Fe-Fe oligomerization takes place, resulting in increased total iron adsorption. Our study highlights the need for more combined experimental-simulation studies on carefully controlled model systems of geochemical relevance, so that the effect of nanoconfinement on the fate of and transport of aqueous metals can further inform geochemical models.

CONFLICT OF INTEREST

There are no conflicts to declare.

ACKNOWLEDGEMENTS

We would like to thank Tuan A. Ho for helpful comments. This work was supported by the US Department of Energy, Office of Science, Office of Basic Energy Sciences, Chemical Sciences, Geosciences and Biosciences Division under Field Work Proposal Number 21-015452. Sandia National Laboratories is a multimission laboratory managed and operated by National Technology and Engineering

Solutions of Sandia, LLC., a wholly owned subsidiary of Honeywell International, Inc., for the U.S. Department of Energy's National Nuclear Security Administration under contract DE-NA-0003525. All X-ray absorption experiments were performed at Sector 20-ID at the Advanced Photon Source (APS), an Office of Science User Facility operated for the U.S. Department of Energy (DOE) Office of Science by Argonne National Laboratory. AGI and AWK thank Austen B. Tigges for assistance with data collection at APS. The views expressed in this article do not necessarily represent the views of the U.S. Department of Energy or the United States Government.

ELECTRONIC SUPPLEMENTARY INFORMATION (ESI)

Supplementary data to this article can be found online.

- Fluid Composition for MD Simulations
- Fe(II) Concentrations and Adsorption Results
- Atomic density profiles
- Analysis of Fe(II) and Fe(III) oligomerization from MD simulations
- Distances and coordination numbers from RDF analysis of MD simulations
- LAMMPS input files

REFERENCES

1 Y. F. Wang, Nanogeochemistry: Nanostructures, emergent properties and their control on geochemical reactions and mass transfers, *Chem. Geol.*, 2014, **378**, 1-23.
2 A. W. Knight, A. B. Tigges and A. G. Ilgen, Adsorption of copper (II) on mesoporous silica: the effect of nano-scale confinement, *Geochem. Trans.*, 2018, **19**, 13.

3 J. Nelson, Bargar, J. R., Wasylenki, L., Brown, G. E., Maher, K., Effects of nano-confinement on Zn(II) adsorption to nanoporous silica, *Geochim. Cosmochim. Acta*, 2018, **240**, 80-97.
4 J. Zachara, S. Brantley, J. Chorover, R. Ewing, S. Kerisit, C. X. Liu, E. Perfect, G. Rother and A. G. Stack, Internal domains of natural porous media revealed: Critical locations for transport, storage, and chemical reaction, *Environ. Sci. Technol.*, 2016, **50**, 2811-2829.
5 A. G. Ilgen, J. E. Heath, I. Y. Akkutlu, L. T. Bryndzia, D. R. Cole, Y. K. Kharaka, T. J. Kneafsey, K. L. Milliken, L. J. Pyrak-Nolte and R. Suarez-Rivera, Shales at all scales: Exploring coupled processes in mudrocks, *Earth-Sci. Rev.*, 2017, **166**, 132-152.
6 A. R. Zimmerman, J. Chorover, K. W. Goyne and S. L. Brantley, Protection of mesopore-adsorbed organic matter from enzymatic degradation, *Environ. Sci. Technol.*, 2004, **38**, 4542-4548.
7 Y. H. Kim, C. M. Kim, I. H. Choi, S. Rengaraj and J. H. Yi, Arsenic removal using mesoporous alumina prepared via a templating method, *Environ. Sci. Technol.*, 2004, **38**, 924-931.
8 P. Huber, Soft matter in hard confinement: phase transition thermodynamics, structure, texture, diffusion and flow in nanoporous media, *J. Phys. Condens. Matter*, 2015, **27**, 103102.
9 T. A. Ho, D. Argyris, D. R. Cole and A. Striolo, Aqueous NaCl and CsCl Solutions Confined in Crystalline Slit-Shaped Silica Nanopores of Varying Degree of Protonation, *Langmuir*, 2012, **28**, 1256-1266.
10 R. Renou, A. Ghoufi, A. Szymczyk, H. Zhu, J. C. Neyt and P. Malfreyt, Nanoconfined Electrolyte Solutions in Porous Hydrophilic Silica Membranes, *J. Phys. Chem. C*, 2013, **117**, 11017-11027.
11 K. Yamashita and H. Daiguji, Molecular Dynamics Simulations of Water Uptake into a Silica Nanopore, *J. Phys. Chem. C*, 2015, **119**, 3012-3023.
12 T. Takei, K. Mukasa, M. Kofuji, M. Fuji, T. Watanabe, M. Chikazawa and T. Kanazawa, Changes in density and surface tension of water in silica pores, *Colloid Polym. Sci.*, 2000, **278**, 475-480.
13 J. B. Brubach, A. Mermet, A. Filabozzi, A. Gerschel, D. Lairez, M. P. Krafft and P. Roy, Dependence of water dynamics upon confinement size, *J Phys. Chem. B*, 2001, **105**, 430-435.
14 S. Le Caer, S. Pin, S. Esnouf, Q. Raffy, J. P. Renault, J. B. Brubach, G. Creff and P. Roy, A trapped water network in nanoporous material: the role of interfaces, *Phys. Chem. Chem. Phys.*, 2011, **13**, 17658-17666.
15 A. W. Knight, N. G. Kalugin, E. Coker and A. G. Ilgen, Water properties under nano-scale confinement, *Sci. Rep.*, 2019, **9**, 8246.
16 J. Marti, G. Nagy, E. Guardia and M. C. Gordillo, Molecular dynamics simulation of liquid water confined inside graphite channels: Dielectric and dynamical properties, *J. Phys. Chem. B*, 2006, **110**, 23987-23994.
17 S. Senapati and A. Chandra, Dielectric Constant of Water Confined in a Nanocavity, *J. Phys. Chem. B*, 2001, **105**, 5106-5109.
18 M. D. Fayer and N. E. Levinger, Analysis of Water in Confined Geometries and at Interfaces, *Annu. Rev. Anal. Chem.*, 2010, **3**, 89-107.
19 I. C. Bourg and J. B. Ajo-Franklin, Clay, Water, and Salt: Controls on the Permeability of Fine-Grained Sedimentary Rocks, *Acc. Chem. Res.*, 2017, **50**, 2067-2074.

20 L. M. Keller, P. Schuetz, R. Erni, M. D. Rossell, F. Lucas, P. Gasser and L. Holzer, Characterization of multi-scale microstructural features in Opalinus Clay, *Micropor. Mesopor. Mater.*, 2013, **170**, 83-94.
21 S. A. Yamada, S. T. Hung, W. H. Thompson and M. D. Fayer, Effects of pore size on water dynamics in mesoporous silica, *J. Chem. Phys.*, 2020, **152**, 154704.
22 H. S. Senanayake, J. A. Greathouse, A. G. Ilgen and W. H. Thompson, Simulations of the IR and Raman spectra of water confined in amorphous silica slit pores, *J. Chem. Phys.*, 2021, **154**, 104503.
23 C. C. Fuller, J. A. Davis, J. A. Coston and E. Dixon, Characterization of metal adsorption variability in a sand and gravel aquifer, Cape Cod, Massachusetts, USA, *J. Contam. Hydrol.*, 1996, **22**, 165-187.
24 X. Ying and L. Axe, Synthesis and characterization of iron oxide-coated silica and its effect on metal adsorption, *J. Colloid Interface Sci.*, 2005, **282**, 11-19.
25 D. Y. Zhao, J. L. Feng, Q. S. Huo, N. Melosh, G. H. Fredrickson, B. F. Chmelka and G. D. Stucky, Triblock copolymer syntheses of mesoporous silica with periodic 50 to 300 angstrom pores, *Science*, 1998, **279**, 548-552.
26 D. Y. Zhao, Q. S. Huo, J. L. Feng, B. F. Chmelka and G. D. Stucky, Nonionic triblock and star diblock copolymer and oligomeric surfactant syntheses of highly ordered, hydrothermally stable, mesoporous silica structures, *J. Am. Chem. Soc.*, 1998, **120**, 6024-6036.
27 L. T. Zhuravlev, The surface chemistry of amorphous silica. Zhuravlev model, *Colloids Surf. A Physicochem. Eng. Asp.*, 2000, **173**, 1-38.
28 C. M. Koretsky, D. A. Sverjensky and N. Sahai, A model of surface site types on oxide and silicate minerals based on crystal chemistry: Implications for site types and densities, multi-site adsorption, surface infrared spectroscopy, and dissolution kinetics, *Am. J. Sci.*, 1998, **298**, 349-438.
29 M. Kruk, M. Jaroniec, C. H. Ko and R. Ryoo, Characterization of the porous structure of SBA-15, *Chem. Mater.*, 2000, **12**, 1961-1968.
30 G. A. Parks, Isoelectric Points of Solid Oxides Solid Hydroxides and Aqueous Hydroxo Complex Systems, *Chem. Rev.*, 1965, **65**, 177-198.
31 R. P. Abendroth, Surface Charge Development on Porous Silica in Aqueous-Solution, *J. Phys. Chem.*, 1972, **76**, 2547-2549.
32 A. W. Knight, P. Ilani-Kashkouli, J. A. Harvey, J. A. Greathouse, T. A. Ho, N. Kabengi and A. G. Ilgen, Interfacial reactions of Cu(II) adsorption and hydrolysis driven by nano-scale confinement, *Environ. Sci. Nano*, 2020, **7**, 68-80.
33 A. G. Ilgen, N. Kabengi, K. Leung, I.-K. Poorandokht, A. W. Knight and L. Loera, Defining silica–water interfacial chemistry under nanoconfinement using lanthanides, *Environ. Sci. Nano*, 2021, **8**, 432-443.
34 R. T. Cygan, J.-J. Liang and A. G. Kalinichev, Molecular Models of Hydroxide, Oxyhydroxide, and Clay Phases and the Development of a General Force Field, *J Phys. Chem. B*, 2004, **108**, 1255-1266.
35 I. C. Bourg and C. I. Steefel, Molecular Dynamics Simulations of Water Structure and Diffusion in Silica Nanopores, *J. Phys. Chem. C*, 2012, **116**, 11556-11564.
36 A. Butenuth, G. Moras, J. Schneider, M. Koleini, S. Koppen, R. Meissner, L. B. Wright, T. R. Walsh and L. C. Ciacchi, Ab initio derived force-field parameters for molecular dynamics

simulations of deprotonated amorphous-SiO2/water interfaces, *Phys. Status Solidi B Basic Solid State Phys.*, 2012, **249**, 292-305.
37 S. H. Chen and S. J. Singer, Molecular Dynamics Study of the Electric Double Layer and Nonlinear Spectroscopy at the Amorphous Silica Water Interface, *J Phys. Chem. B*, 2019, **123**, 6364-6384.
38 M. F. Dopke, J. Lutzenkirchen, O. A. Moultos, B. Siboulet, J. F. Dufreche, J. T. Padding and R. Hartkamp, Preferential Adsorption in Mixed Electrolytes Confined by Charged Amorphous Silica, *J. Phys. Chem. C*, 2019, **123**, 16711-16720.
39 J. Geske, M. Harrach, L. Heckmann, R. Horstmann, F. Klameth, N. Muller, E. Pafong, T. Wohlfromm, B. Drossel and M. Vogel, Molecular Dynamics Simulations of Water, Silica, and Aqueous Mixtures in Bulk and Confinement, *Z. Phys. Chem.*, 2018, **232**, 1187-1225.
40 J. A. Harvey and W. H. Thompson, Thermodynamic Driving Forces for Dye Molecule Position and Orientation in Nanoconfined Solvents, *J Phys. Chem. B*, 2015, **119**, 9150-9159.
41 A. A. Hassanali, H. Zhang, C. Knight, Y. K. Shin and S. J. Singer, The Dissociated Amorphous Silica Surface: Model Development and Evaluation, *J. Chem. Theory Comput.*, 2010, **6**, 3456-3471.
42 S. Leroch and M. Wendland, Simulation of Forces between Humid Amorphous Silica Surfaces: A Comparison of Empirical Atomistic Force Fields, *J. Phys. Chem. C*, 2012, **116**, 26247-26261.
43 A. A. Milischuk and B. M. Ladanyi, Structure and dynamics of water confined in silica nanopores, *J. Chem. Phys.*, 2011, **135**.
44 A. M. Schrader, J. I. Monroe, R. Sheil, H. A. Dobbs, T. J. Keller, Y. X. Li, S. Jain, M. S. Shell, J. N. Israelachvili and S. G. Han, Surface chemical heterogeneity modulates silica surface hydration, *Proc. Natl. Acad. Sci. U. S. A.*, 2018, **115**, 2890-2895.
45 N. W. Suek, M. C. Guillaume, J. Y. P. Delannoy and F. Tielens, Characterization of hydroxylated amorphous silica: a numerical approach, *Adsorption*, 2018, **24**, 267-278.
46 T. T. B. Le, A. Striolo, S. S. Gautam and D. R. Cole, Propane-Water Mixtures Confined within Cylindrical Silica Nanopores: Structural and Dynamical Properties Probed by Molecular Dynamics, *Langmuir*, 2017, **33**, 11310-11320.
47 F. S. Emami, V. Puddu, R. J. Berry, V. Varshney, S. V. Patwardhan, C. C. Perry and H. Heinz, Force Field and a Surface Model Database for Silica to Simulate Interfacial Properties in Atomic Resolution, *Chem. Mater.*, 2014, **26**, 2647-2658.
48 S. J. Plimpton, Fast Parallel Algorithms for Short-Range Molecular Dynamics, *J. Comp. Phys.*, 1995, **117**, 1-19.
49 S. J. Plimpton, R. Pollock and M. Stevens, In *Particle-Mesh Ewald and rRESPA for Parallel Molecular Dynamics Simulations*, Proceedings of the Eighth SIAM Conference on Parallel Processing for Scientific Computing, Minneapolis, MN, 1997.
50 J. M. Rimsza, R. E. Jones and L. J. Criscenti, Surface Structure and Stability of Partially Hydroxylated Silica Surfaces, *Langmuir*, 2017, **33**, 3882-3891.
51 C. D. Daub, N. M. Cann, D. Bratko and A. Luzar, Electrokinetic flow of an aqueous electrolyte in amorphous silica nanotubes, *Phys. Chem. Chem. Phys.*, 2018, **20**, 27838-27848.
52 M. Collin, S. Gin, B. Dazas, T. Mahadevan, J. C. Du and I. C. Bourg, Molecular Dynamics Simulations of Water Structure and Diffusion in a 1 nm Diameter Silica Nanopore as a Function of Surface Charge and Alkali Metal Counterion Identity, *J. Phys. Chem. C*, 2018, **122**, 17764-17776.

53 T. A. Ho, D. Argyris, D. V. Papavassiliou, A. Striolo, L. L. Lee and D. R. Cole, Interfacial water on crystalline silica: a comparative molecular dynamics simulation study, *Mol. Simul.*, 2011, **37**, 172-195.

54 A. A. Chialvo, L. Vlcek and D. R. Cole, Aqueous CO2 Solutions at Silica Surfaces and within Nanopore Environments. Insights from Isobaric-Isothermal Molecular Dynamics, *J. Phys. Chem. C*, 2012, **116**, 13904-13916.

55 Z. Brkljaca, D. Namjesnik, J. Lutzenkirchen, M. Predota and T. Preocanin, Quartz/Aqueous Electrolyte Solution Interface: Molecular Dynamic Simulation and Interfacial Potential Measurements, *J. Phys. Chem. C*, 2018, **122**, 24025-24036.

56 O. Kroutil, Z. Chval, A. A. Skelton and M. Predota, Computer Simulations of Quartz (101)-Water Interface over a Range of pH Values, *J. Phys. Chem. C*, 2015, **119**, 9274-9286.

57 M. Bouhadja and A. A. Skelton, Dynamical Properties of Water and Ions at the Quartz (101)–Water Interface at a Range of Solution Conditions: A Classical Molecular Dynamics Study, *J. Phys. Chem. C*, 2018, **122**, 1535-1546.

58 G. R. Quezada, R. E. Rozas and P. G. Toledo, Molecular Dynamics Simulations of Quartz (101)-Water and Corundum (001)-Water Interfaces: Effect of Surface Charge and Ions on Cation Adsorption, Water Orientation, and Surface Charge Reversal, *J. Phys. Chem. C*, 2017, **121**, 25271-25282.

59 A. A. Skelton, D. J. Wesolowski and P. T. Cummings, Investigating the Quartz $(10\bar{1}0)$/Water Interface using Classical and Ab Initio Molecular Dynamics, *Langmuir*, 2011, **27**, 8700-8709.

60 A. A. Skelton, P. Fenter, J. D. Kubicki, D. J. Wesolowski and P. T. Cummings, Simulations of the Quartz(10(1)over-bar1)/Water Interface: A Comparison of Classical Force Fields, Ab Initio Molecular Dynamics, and X-ray Reflectivity Experiments, *J. Phys. Chem. C*, 2011, **115**, 2076-2088.

61 Y. M. Ma, H. Zhang and B. J. Zhang, Structure of sodium sulphate aqueous solution/quartz interface: a molecular dynamics simulation, *Mol. Simul.*, 2014, **40**, 634-639.

62 M. Pouvreau, J. A. Greathouse, R. T. Cygan and A. G. Kalinichev, Structure of Hydrated Kaolinite Edge Surfaces: DFT Results and Further Development of the ClayFF Classical Force Field with Metal–O–H Angle Bending Terms, *J. Phys. Chem. C*, 2019, **123**, 11628-11638.

63 J. A. Harvey, C. T. Johnston, L. J. Criscenti and J. A. Greathouse, Distinguishing between bulk and edge hydroxyl vibrational properties of 2 : 1 phyllosilicates via deuteration, *Chem. Commun.*, 2019, **55**, 3453-3456.

64 O. Teleman, B. Jonsson and S. Engstrom, A Molecular Dynamics Simulation of a Water Model with Intramolecular Degrees of Freedom, *Mol. Phys.*, 1987, **60**, 193-203.

65 E. Brodskaya, A. P. Lyubartsev and A. Laaksonen, Investigation of water clusters containing OH- and H3O+ ions in atmospheric conditions. A molecular dynamics simulation study, *J Phys. Chem. B*, 2002, **106**, 6479-6487.

66 D. R. Smith and L. X. Dang, Computer Simulations of NaCl Association in Polarizable Water, *J. Chem. Phys.*, 1994, **100**, 3757-3766.

67 C. S. Babu and C. Lim, Empirical force fields for biologically active divalent metal cations in water, *J. Phys. Chem. A*, 2006, **110**, 691-699.

68 K. Ando, Solvent nuclear quantum effects in electron transfer reactions. III. Metal ions in water. Solute size and ligand effects, *J. Chem. Phys.*, 2001, **114**, 9470-9477.

69 M. Kosmulski, pH-dependent surface charging and points of zero charge. IV. Update and new approach, *J. Colloid Interface Sci.*, 2009, **337**, 439-448.

70 O. S. Smart, J. G. Neduvelil, X. Wang, B. A. Wallace and M. S. P. Sansom, HOLE: A program for the analysis of the pore dimensions of ion channel structural models, *J. Mol. Graph. Model.*, 1996, **14**, 354-360.

71 I. C. Yeh and M. L. Berkowitz, Ewald summation for systems with slab geometry, *J. Chem. Phys.*, 1999, **111**, 3155-3162.

72 B. Ravel and M. Newville, ATHENA, ARTEMIS, HEPHAESTUS: data analysis for X-ray absorption spectroscopy using IFEFFIT, *J. Synchrotron Radiat.*, 2005, **12**, 537-541.

73 M. Newville, IFEFFIT: interactive XAFS analysis and FEFF fitting, *J. Synchrotron Radiat.*, 2001, **8**, 322-324.

74 S. Kelly, D. Hesterberg and B. Ravel: Analysis of Soils and Minerals Using X-ray Absorption Spectroscopy. In *Methods of Soil Analysis: Part 5--Mineralogical Methods*, A. Ulery and L. Drees, Eds., Soil Science Society of America, Madison, WI, USA, 2008, 387-465.

75 S. I. Zabinsky, J. J. Rehr, A. Ankudinov, R. C. Albers and M. J. Eller, Multiple-scattering calculations of X-ray-absorption spectra, *Phys. Rev. B*, 1995, **52**, 2995-3009.

76 A. Manceau, D. Chateigner and W. Gates, Polarized EXAFS, distance-valence least-squares modeling (DVLS), and quantitative texture analysis approaches to the structural refinement of Garfield nontronite, *Phys. Chem. Miner.*, 1998, **25**, 347-365.

77 F. J. Millero, W. Yao and J. Aicher, The speciation of Fe(II) and Fe(III) in natural waters, *Mar. Chem.*, 1995, **50**, 21-39.

78 K. Saeki, Adsorption of Fe^{2+} and Mn^{2+} on silica, gibbsite, and humic acids, *Soil Sci.*, 2004, **169**, 832-840.

79 J. A. Greathouse, R. T. Cygan, J. T. Fredrich and G. R. Jerauld, Adsorption of Aqueous Crude Oil Components on the Basal Surfaces of Clay Minerals: Molecular Simulations Including Salinity and Temperature Effects, *J. Phys. Chem. C*, 2017, **121**, 22773-22786.

80 P. W. Schindler, B. Furst, R. Dick and P. U. Wolf, Ligand Properties of Surface Silanol Groups .1. Surface Complex-Formation with Fe^{3+}, Cu^{2+}, Cd^{2+}, and Pb^{2+}, *J. Colloid Interface Sci.*, 1976, **55**, 469-475.

81 M. Q. Zhu, B. W. Puls, C. Frandsen, J. D. Kubicki, H. Z. Zhang and G. A. Waychunas, In Situ Structural Characterization of Ferric Iron Dimers in Aqueous Solutions: Identification of mu-Oxo Species, *Inorg. Chem.*, 2013, **52**, 6788-6797.

82 C. M. Flynn, Hydrolysis of Inorganic Iron(III) Salts, *Chem. Rev.*, 1984, **84**, 31-41.

83 S. F. Cheah, G. E. Brown and G. A. Parks, XAFS spectroscopy study of Cu(II) sorption on amorphous SiO2 and gamma-Al2O3: Effect of substrate and time on sorption complexes, *J. Colloid Interface Sci.*, 1998, **208**, 110-128.

84 T. P. Trainor, G. E. Brown and G. A. Parks, Adsorption and Precipitation of Aqueous Zn(II) on Alumina Powders, *J. Colloid Interface Sci.*, 2000, **231**, 359-372.

85 G. S. Pokrovski, J. Schott, F. Garges and J. L. Hazemann, Iron (III)-silica interactions in aqueous solution: Insights from X-ray absorption fine structure spectroscopy, *Geochim. Cosmochim. Acta*, 2003, **67**, 3559-3573.

86 Y. S. Jun, B. Lee and G. A. Waychunas, In Situ Observations of Nanoparticle Early Development Kinetics at Mineral-Water Interfaces, *Environ. Sci. Technol.*, 2010, **44**, 8182-8189.